Materials Horizons

ROYAL SOCIETY OF CHEMISTRY

COMMUNICATION

View Article Online
View Journal | View Issue

Cite this: *Mater. Horiz.*, 2025, 12, 8603

Received 30th April 2025,
Accepted 10th July 2025

DOI: 10.1039/d5mh00815h

rsc.li/materials-horizons

A photothermal-driven hydrovoltaic-pyroelectric hybrid system for efficient energy harvesting and self-powered disinfection†

Hui Cheng,[ab] Hiang Kwee Lee *[cd] and Haitao Li*[a]

Capturing energy from water phase transitions holds great promise in emerging energy technologies due to its green, sustainable, and abundant nature. However, effectively harvesting this energy remains challenging, largely due to the inherently slow evaporation of water. Here, we present a high-performance hybrid generator that efficiently extracts water-phase transition energy through a multiscale structural design. The system integrates an arched multifunctional film with a polarized PVDF layer, enabling simultaneous photothermal, hydrovoltaic, and pyroelectric energy harvesting. Under optimized conditions, the device achieves a photothermal evaporation rate of ~1.53 kg m^{-2} h^{-1} with a conversion efficiency of ~96% enabled by rational microcomponent regulation, which is ~30% higher than its planar counterpart. The hydrovoltaic output reaches a V_{OC} value of ~1.13 V and an I_{SC} value of ~6.46 μA, delivering a power density of ~611 μW m^{-2} that is 8.5-fold higher than previous designs under 1 sun illumination in seawater. The generator also yields a pyroelectric V_{OC} value of ~143 V and an I_{SC} value of ~694 nA, with a peak power density of ~13.58 mW m^{-2}. Notably, these electrical outputs surpass earlier reports by >80%, attributed to enhanced interfacial temperature oscillations driven by the arched geometry. This platform reliably powers small electronic devices and enables a self-driven electrocatalytic system for seawater disinfection, achieving sodium hypochlorite production by coupling the generator with commercial Pt electrodes. Our multiscale design offers new insights for developing self-sustaining energy systems capable of harvesting and converting water-based energy for practical applications.

New concepts

This study introduces a multiscale design strategy that enables efficient, continuous harvesting of water phase transition energy by combining microscale material regulation with macroscale geometric structuring. Unlike conventional systems that rely on a single energy conversion pathway or planar configurations, this hybrid platform integrates hydrovoltaic and pyroelectric effects within a single device architecture, enhancing both energy density and adaptability to ambient solar and water sources. The work also demonstrates a self-powered electrocatalytic system capable of producing disinfectants directly from seawater, showcasing the platform's real-world functionality. Beyond performance, the approach offers a transferable design principle for coupling multiple interfacial energy mechanisms in material systems. This provides new insight into how integrated micro/nanostructuring can be applied to design energy-autonomous systems with direct environmental and chemical utility. The concept has implications for advancing decentralized energy–water technologies and broadens the framework for ambient energy harvesting in underexplored domains.

1. Introduction

Self-driving energy-generating nanosystems are gaining increasing attention across diverse fields, including catalysis,[1,2] display technologies,[3,4] and IoT sensing,[5,6] due to their high flexibility, portability, responsiveness, and reliable ability to harvest ambient energy.[7,8] Among various energy carriers, water stands out for its abundance and environmental sustainability. For example, traditional hydroelectric systems that utilize water's potential energy have inspired the design of next-generation self-powered platforms. Additionally, water serves as an excellent carrier of thermal energy due to its high specific heat capacity and phase change enthalpy.[9,10] Emerging technologies increasingly harness the thermal energy stored in water to drive power generation, particularly through hydrovoltaic[11–13] and pyroelectric[14–16] mechanisms. However, the naturally slow evaporation of water limits energy extraction efficiency. Hence, developing more efficient water-based power generation methods remains a critical challenge.

[a] *Academy for Advanced Interdisciplinary Studies, Nanjing Agricultural University, Nanjing 210095, China. E-mail: haitaoli@njau.edu.cn*
[b] *School of Chemistry and Chemical Engineering, Yangzhou University, Yangzhou, 225002, P. R. China*
[c] *Division of Chemistry and Biological Chemistry, School of Chemistry, Chemical Engineering and Biotechnology, Nanyang Technological University, 21 Nanyang Link, 637371, Singapore. E-mail: hiangkwee@ntu.edu.sg*
[d] *Institute of Materials Research and Engineering, The Agency for Science, Technology and Research (A*STAR), 2 Fusionopolis Way, #08-03, Innovis, 138634, Singapore*
† Electronic supplementary information (ESI) available. See DOI: https://doi.org/10.1039/d5mh00815h

Low-carbon photothermal technologies offer a promising approach to enhance water evaporation efficiency and improve power generation performance when using water as an energy carrier. Inspired by the self-regulating behavior of human skin,[16] Shang *et al.* developed a system that integrates tungsten-doped vanadium dioxide nanoparticles as the evaporative interface with a polarized PVDF film as the pyroelectric layer. Under solar radiation, this design induces strong temperature oscillations and effectively captures phase transition energy during evaporation. Previous studies[17–19] also demonstrated that coupling photothermal technology with hydrovoltaic systems enhances power output by accelerating water molecule flow through nano- and micro-channels. However, relying on a single power generation mechanism often fails to fully harvest the various forms of energy stored in water, including thermally driven molecular motion and latent heat.

To overcome this limitation, we previously proposed a water energy co-capture strategy that integrates hydrovoltaic and pyroelectric effects,[20] achieving a 22.6-fold increase in power output compared to conventional hydrovoltaic devices. Despite this improvement, the prior system – based on planar carbon black (CB) photothermal layers – still suffers from limited power generation efficiency. This limitation arises from two key factors: (1) CB's inherently low zeta potential restricts its hydrovoltaic activity, and (2) its weak infrared absorption, combined with a flat structure and limited evaporation area, reduces the overall photothermal evaporation rate. Therefore, it is essential to develop advanced functional layers that combine strong photothermal and electroactive properties to simultaneously boost evaporation dynamics and hydrovoltaic performance.

Herein, we present a multifunctional hybrid generator with a multiscale architecture that maximizes energy harvesting from water through rational structural and material designs. The system features a strategically designed arched multifunctional film coupled with a polarized PVDF film, where each component is specifically engineered to enhance energy conversion efficiency. The upper multifunctional film exhibits high photothermal and hydrovoltaic performance, enabled by its precisely controlled hierarchical design. At the microscale, we achieve superior photo- and electro-activity by integrating carbon nanotubes (CNTs) and carbon black (CB) into our hybrid platform. The CNTs provide efficient charge transport pathways while the CB nanoparticles ensure broadband light absorption, jointly driving the effective photogeneration and migration of charge carriers. This optimized material system is fabricated as a CB/CNT@BFP composite by uniformly depositing the hybrid CB/CNT coating onto bamboo fiber paper (BFP), resulting in both excellent conductivity and mechanical robustness. More importantly, the macroscale arched structure of the CB/CNT@BFP film effectively amplifies interfacial temperature gradients during photothermal evaporation, which is crucial for boosting the pyroelectric response of the underlying PVDF layer. Through this multiscale approach, our multifunctional design achieves enhanced energy harvesting efficiency by simultaneously leveraging and amplifying hydrovoltaic and pyroelectric effects under solar irradiation, offering valuable insights into how the synergy between material composition and structural architecture can elevate device performance in energy conversion systems.

Under optimized conditions, our design achieves a photothermal evaporation rate of $\sim$1.53 kg m^{-2} h^{-1} with an efficiency of $\sim$96%, $\sim$30% higher than the planar configuration. This enhanced performance arises from improved microscopic component properties achieved *via* rationally combining CB and CNTs. Moreover, the hydrovoltaic open-circuit voltage (V_{OC}) and short-circuit current (I_{SC}) reach $\sim$1.13 V and $\sim$6.46 μA, respectively, delivering a power density of $\sim$611 μW m^{-2} that is 8.5-fold higher than that of our previous device under 1 sun illumination in seawater. The hybrid generator also produces a pyroelectric V_{OC} of $\sim$143 V and an I_{SC} of $\sim$694 nA, with a peak power density of $\sim$13.58 mW m^{-2}. Notably, this output exceeds previous reports by $>$80%, attributed to enhanced temperature oscillations enabled by the arched design. Our power-generating device reliably powers small electronic devices, such as LED lamps and calculators. As a proof of concept, we further construct a self-driven electrocatalytic device for disinfectant production by coupling the hybrid generator with two commercial Pt electrodes. This self-powered system successfully generates $\sim$4.67 g of sodium hypochlorite after 72 hours of operation in seawater. Our design offers valuable insights for developing self-sustained energy systems that harvest and convert water-based energy for practical applications.

2. Experimental

2.1. Materials

Polyvinylidene fluoride (PVDF, MW = 900 000, used as an adhesive) and acetone (99%) were purchased from Shanghai Aladdin Biochemical Technology Co., Ltd. Sodium chloride (NaCl, 99.5%) and ethanol (99.5%) were purchased from Sigma-Aldrich. The polarized PVDF pyroelectric film was purchased from Measurement Specialties Inc. (USA) and was precoated with silver (Ag) electrodes at a thickness of 6 μm. All chemicals were of analytical grade and were used without further purification. Carbon black powders (CB, 4500 mesh), hydroxylated carbon nanotubes (CNT), seawater, glass spray bottles (20 mL), a resistance package (1 kΩ–500 MΩ) and other conductive materials were purchased from an online retailer *via* Alibaba.

2.2. Preparation of CB/CNT@BFP films

CB/CNT@BFP films were prepared using a simple spraying method. Carbon nanotubes (CNTs) and carbon black (CB) were mixed at a ratio of 1 : 10, and the resulting CB/CNT mixture was combined with PVDF powder at a mass ratio of 0.45 : 1 (CB/CNT : PVDF). The PVDF powder (0.15 g) was first dispersed in acetone (18.6 mL; PVDF : acetone = 1 : 100) and stirred using a magnetic stirrer until the solution became transparent. Subsequently, CB (60 mg) and CNTs (6 mg) were added to the solution and homogenized *via* ultrasonication to obtain a uniform precursor dispersion. The resulting CB/CNT solution was sprayed onto a bamboo fiber paper (BFP) substrate

($70 \times 160 \times 0.35$ mm^3) and dried under ambient conditions. After drying, the CB/CNT@BFP film was cut into rectangular strips (30×70 mm^2), and two iron (Fe) electrodes were connected at both ends of the film for solar thermal conversion and evaporation-induced power generation measurements.

2.3. Construction of the hybrid generator

A polarized PVDF pyroelectric film (20×20 mm^2) was adhered to the CB/CNT@BFP film using transparent adhesive tape. A piece of water-absorbing paper was inserted from one end of the hydrophilic CB/CNT@BFP surface into the water reservoir, functioning as a water transport channel. The assembled hybrid device was connected to a digital ammeter to measure real-time voltage and current under simulated solar irradiation.

2.4. Instruments and characterization

The morphology and surface structure of BFP, CB, CNT, CB/CNT@BFP, and PVDF films were characterized using a field emission scanning electron microscope (Zeiss SEM) operating at an accelerating voltage of 5 kV. The specific surface area and pore size were measured using BET analysis (Beishide 3H-2000PS2). Surface functional groups and chemical bonding states were analyzed by Fourier transform infrared spectroscopy (FTIR). Surface temperature measurements of the CB/CNT@BFP film were performed using an infrared thermal imager (FLIR E5, USA) and a temperature change gauge (EH-ME020, China). UV-Vis-NIR absorption spectra of the photothermal layers were recorded in the 200–2500 nm range using a Cary 5000 spectrophotometer (Varian Co., Japan). CB and CNTs were qualitatively analyzed using powder X-ray diffraction (XRD) on a Bruker diffractometer (Germany) over a 2θ range of 10–80°. The real-time open-circuit voltage (V_{OC}) and short-circuit current (I_{SC}) were recorded using a Keithley 2450/6517A multimeter and an EH-ME010 device (China). Wettability was evaluated through water contact angle (WCA) measurements. The pyroelectric properties of the polarized PVDF film were examined using piezoresponse force microscopy (PFM) and Kelvin probe force microscopy (KPFM) modules in atomic force microscopy (AFM, SPA-300HV). The zeta potentials of CB and CNTs were measured using a nanoparticle size analyzer (ZEN 3690, Malvern Instruments, UK). The concentration of hypochlorite (ClO^-) was measured using a residual chlorine detector (LH-C01, China).

3. Results and discussion

The design principles and fabrication of our distinct self-driven power-generating device for disinfectant synthesis by using the energy extracted from water are illustrated in Fig. 1. This integrated design comprises a hybrid power generator coupled with two platinum electrodes that function as the catalytic module. The upper layer of the generator consists of a multifunctional composite film that enables both photothermal evaporation and electricity generation, fabricated *via* a simple spray-coating method (Fig. 1a). Specifically, carbon black and carbon nanotubes (CB/CNT) serve as photo- and electro-active

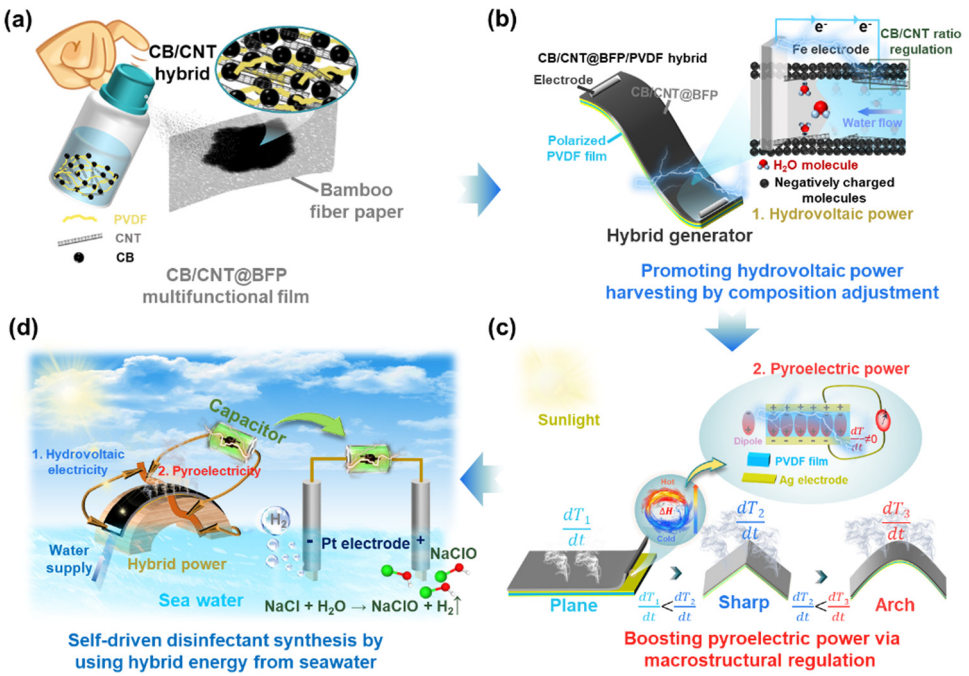

Fig. 1 Schematic illustration of the design and application of a self-driven power-generating device for disinfectant production. (a) Fabrication of CB/CNT@BFP multifunctional films *via* a spray-coating method and (b) assembly of the CB/CNT@BFP hybrid generator enabling water-induced power generation by microcomponent regulation. (c) Enhancement of pyroelectric energy harvesting during interfacial evaporation by employing macroscopic structural optimization. (d) Operation of the hybrid generator for disinfectant production by capturing seawater phase change energy to drive the electrocatalytic formation of sodium hypochlorite.

materials, with acetone as the dispersant, PVDF as the adhesive, and hydrophilic bamboo fiber paper (BFP) as the substrate. Through asymmetric spraying, we obtain a Janus-structured CB/CNT@BFP film capable of concurrently facilitating both photothermal evaporation and hydrovoltaic electricity generation. Notably, the optical and electrical properties of the multifunctional film, including its photothermal and hydrovoltaic output, can be effectively enhanced through the microscopic regulation of the CB/CNT composition (Fig. 1b). A commercial polarized PVDF film, pre-coated with silver electrodes, is positioned beneath the multifunctional layer to function as the pyroelectric component, harvesting energy from thermal fluctuations during water phase transitions. To further increase the interfacial evaporation and enhance pyroelectric recovery, a macroscopic arched structure is introduced into the film architecture (Fig. 1c). Finally, the fully assembled hybrid system that integrates the CB/CNT@BFP generator with two commercial Pt electrodes enables continuous, self-driven seawater electrolysis. This setup captures phase change energy from seawater and converts it into electrical energy to drive the *in situ* synthesis of sodium hypochlorite, a widely used disinfectant (Fig. 1d).

We choose commercially available carbon black (4500 mesh) and hydroxylated carbon nanotubes (CNTs) as key photoactive and electroactive components to fabricate the CB/CNT@BFP multifunctional film. These materials offer excellent photothermal and electrical properties, which we tune through a simple composite strategy. To analyze their composition and structure, we first perform FTIR on CB and CNT, as shown in Fig. 2a. Both materials exhibit polar (–OH) and dissociative (–COOH) functional groups,[8,21] which are essential for hydrovoltaic activity under water supply conditions. The surface chemistries of both materials are further verified using X-ray photoelectron spectroscopy (XPS; Fig. S1, ESI†). We also measure the Zeta potential of CB, CNT, and the CB/CNT composite (Fig. S2, ESI†). The composite shows a potential of −18.3 mV, between CB (−7.6 mV) and CNT (−42.6 mV), indicating that adjusting the composite ratio effectively tunes the surface charge and electroactive behavior. In addition, we evaluate the specific surface area using Brunauer–Emmett–Teller (BET) analysis (Fig. 2b), since surface area directly impacts ion exchange in hydrovoltaic power generation. CNT shows a higher surface area (116.4 $m^2 g^{-1}$) due to its tubular structure, while CB records a lower value (61.9 $m^2 g^{-1}$). The CB/CNT composite achieves an intermediate surface area of 89.8 $m^2 g^{-1}$, offering a balanced structure that optimizes the surface area along with electroactive and photothermal properties. Collectively, our composite strategy enables precise control over the microscopic properties of electroactive components, which is critical for enhancing the performance of the multifunctional film.

Notably, we observe that CB shows stronger absorption in the ultraviolet and visible light regions, while CNT exhibits superior light-harvesting capability in the infrared range, confirming their optical complementarity (Fig. 2c). As a result, the CB/CNT composite demonstrates the most balanced and broad-spectrum light absorption, which could potentially play a critical role in enhancing the photothermal properties of the functional film compared to pure CB or CNT. Moreover, we use hydrophilic bamboo fiber paper (BFP) as the substrate, which facilitates water transport due to its abundant hydrophilic groups and porous fiber structure. FTIR analysis (inset of Fig. 2d)

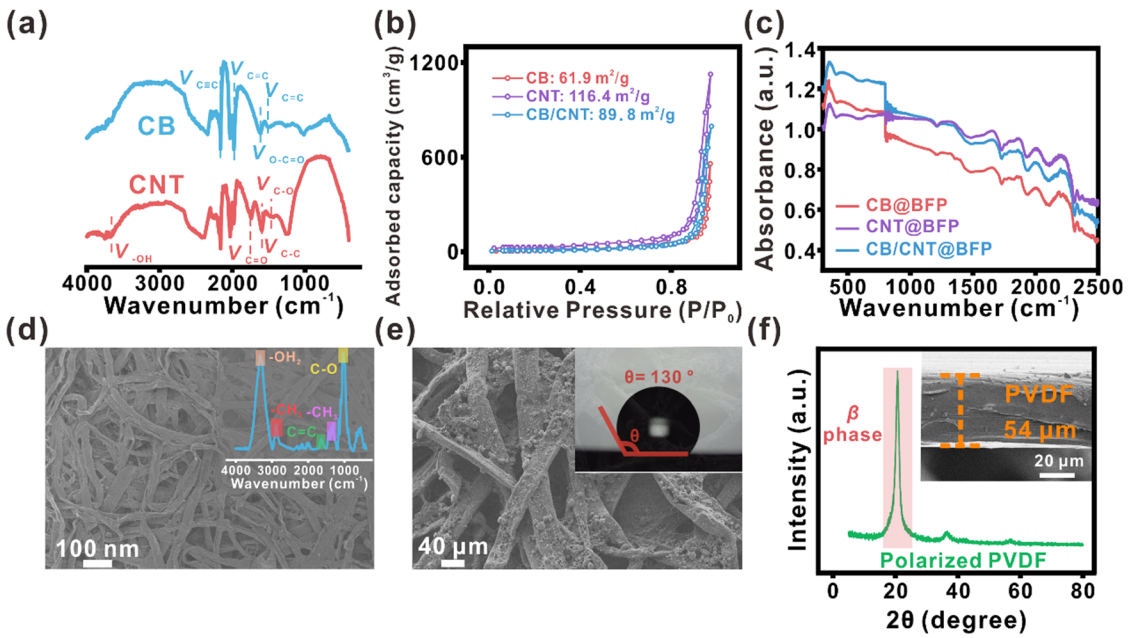

Fig. 2 Physical and chemical structural characterization of the CB/CNT@BFP power generator. (a) FTIR spectra of CB and CNT, (b) N_2 gas adsorption–desorption isotherms and (c) UV-Vis-NIR absorption spectra of CB, CNT, and the CB/CNT hybrid. SEM images of (d) pure BFP (inset: FTIR of BFP) and (e) CB/CNT@BFP film (inset: water contact angle on the CB/CNT-loaded surface). (f) XRD spectrum of the polarized PVDF film (inset: cross-sectional SEM image of the PVDF film).

confirms the presence of these groups. Additionally, the porosity of the BFP was assessed using BET analysis by measuring its specific surface area. The results reveal a specific surface area of 0.955 m^2 g^{-1}, confirming its suitability for efficient water transport and vapor exchange (Fig. S3a, ESI†). To evaluate mechanical performance, we carried out tensile stress–strain measurements. The results indicate that BFP exhibits a fracture strength exceeding 5 MPa (Fig. S3b, ESI†), which ensures mechanical robustness and structural integrity during prolonged operational cycles.

The CB/CNT@BFP film, fabricated *via* spray coating, shows hydrophobicity on the loaded side, attributed to the intrinsic hydrophobic nature of CB and CNT (inset of Fig. 2e). SEM images in Fig. 2e and Fig. S4b (ESI†) reveal that the CB/CNT composite forms a relatively uniform coating on the BFP surface. We use hydrophobic PVDF as an adhesive to bind the CB/CNT to the substrate. This Janus-structured CB/CNT@BFP film serves as the upper layer of our hybrid generator, providing dual functionality in electricity generation and photothermal conversion. The bottom layer consists of a polarized PVDF film with a thickness of 54 μm (inset of Fig. 2f). This PVDF layer exhibits strong pyroelectric performance, with a high polar β-phase content of ~93%, as confirmed by XRD (Fig. 2f) and calculated by FTIR (Fig. S6, ESI†). The polarized PVDF is crucial for enabling the efficient capture of the fluctuating thermal energy *via* the Ag electrodes deposited on the PVDF surface.

The carbon-based composite loaded onto the BFP substrate serves two key roles: it provides both photothermal activity and electroactive functionality. We enhance the properties of the CB/CNT@BFP film by regulating its microscopic composition through a rational combination of CB and CNT. To evaluate photothermal performance, we use an infrared (IR) camera to monitor surface temperatures of different carbon-based films under continuous 1 sun illumination for 2 minutes (25 °C, 55% RH). As shown in Fig. 3a and Fig. S8a (ESI†), the CB/CNT composite reaches the highest surface temperature (63.0 °C), outperforming both pure CB and CNT. This improvement results from synergistic light absorption and enhanced thermal confinement effects. This superior photothermal effect arises due to three main reasons. (1) The composite forms a multiscale porous architecture where CB particles fill the interstitial spaces of the CNT network. This configuration introduces multiple internal light-scattering events, effectively extending the photon path length and enhancing light absorption, as supported in prior reports.[22] (2) The CB and CNT exhibit complementary optical absorption across the solar spectrum, as shown in Fig. 2c. CB primarily absorbs strongly in the UV-visible region, whereas CNTs offer stronger absorption in the near-infrared region. The CB/CNT hybrid thus integrates these spectral advantages to achieve broader and more effective solar energy harvesting. (3) In addition to optical enhancement, the composite structure promotes thermal synergy. CB's relatively low thermal conductivity (<1 W m^{-1} K^{-1}) allows for rapid localized heat accumulation, while the high thermal conductivity of CNTs (>3000 W m^{-1} K^{-1}) facilitates efficient lateral heat distribution across the film. This combination minimizes thermal dissipation and leads to a more uniform and elevated surface temperature under illumination. Together, these

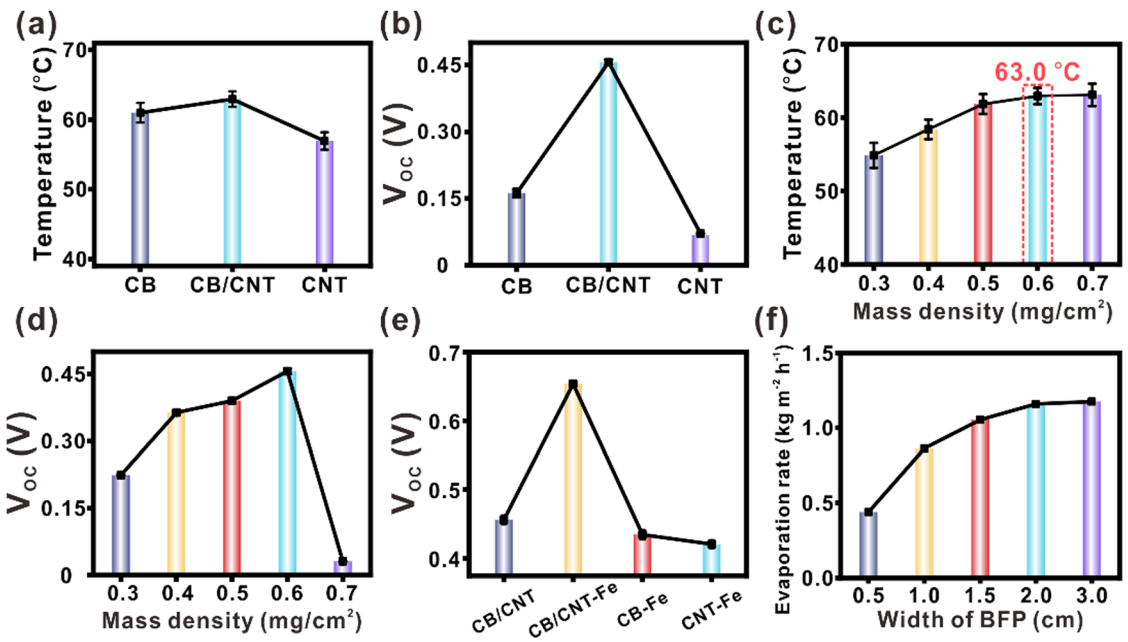

Fig. 3 Interface photothermal and electricity generation performance of various carbon-based films. (a) Photothermal temperature of the film based on the CB, CNT, and CB/CNT mixture (CB : CNT = 10 : 1) under 1 sun illumination for 2 min (carbon loading: 0.6 mg cm^{-2}). (b) Corresponding hydrovoltaic voltage output for each film. (c) Photothermal temperature and (d) hydrovoltaic voltage of the CB/CNT hybrid with varying loadings (0.3–0.7 mg cm^{-2}). (e) Hydrovoltaic voltage generated by functional films using Fe electrodes with CB, CNT, and CB/CNT coatings. (f) Photothermal evaporation performance of CB/CNT@BFP films using BFP strips of varying widths as water supply channels (1 sun, 25 °C, 55% RH).

optical and thermal synergies account for the superior photothermal performance of the CB/CNT composite over either component individually.

In addition, the composite structure also drastically enhances the hydrovoltaic properties of the film (Fig. 3b). The hydrovoltaic effect refers to electricity generation through interfacial interactions between water and nanomaterials.[23] This phenomenon arises from interfacial interactions between water molecules and electroactive nanomaterials. When water contacts the CB/CNT-coated BFP surface, dissociable functional groups (*e.g.*, –OH, –COOH) on the carbon materials generate mobile protons. As water continuously evaporates, capillary action and transpiration create a directional flow of water and ions across the film. This movement establishes a proton gradient and leads to the formation of an electrokinetic potential, which drives continuous electricity generation. Notably, the open-circuit voltage (V_{OC}) of the CB/CNT film is at least 185% higher than that of either pure CB or CNT, driven by optimized surface charge and conductivity at the microscopic level. We conducted additional experiments to systematically investigate the influence of different CNT:CB mass ratios (1 : 0, 7 : 3, 1 : 1, 1 : 10, and 0 : 1) on the overall energy harvesting performance of our CB/CNT@BFP film. The corresponding results are presented in Fig. S7 (ESI†). Our data clearly show that as the proportion of CB increases, the power output of the device consistently improves, reaching a peak value (~1827 nW) when the CB content is 90% (*i.e.*, a CNT : CB ratio of 1 : 10). Beyond this ratio, further increasing CB does not yield noticeable gains, and may hinder electron transport due to insufficient CNT network formation. This balance reflects the complementary roles of CNTs and CB in our composite, whereby CNTs provide a conductive backbone for efficient charge transport while CB ensures strong broadband light absorption and thermal localization.

Furthermore, to determine the optimal loading of the CB/CNT composite, we examine its effect on both photothermal and hydrovoltaic performance, as shown in Fig. 3c. As the composite loading increases, the surface temperature rises and plateaus at 0.6 mg cm^{-2}. Under the same conditions (25 °C, 55% RH), the hydrovoltaic voltage also peaks at ~0.45 V (Fig. 3d). These observations reflect a balance between material activity and water transport. At low loading, the film lacks sufficient ion exchange interfaces and active surface area for efficient charge generation. At high loading, the hydrophobic nature of CB and CNT impedes water transport, suppressing evaporation and reducing power output. Both extremes, therefore, limit overall performance. Our findings identify 0.6 mg cm^{-2} as the optimal CB/CNT loading to achieve high-efficiency photothermal and hydrovoltaic output in the bifunctional film.

To further enhance water-induced electricity generation, we introduce a galvanic effect by installing Fe electrodes on the surface of the CB/CNT@BFP film (Fig. 3e). Notably, the synergy between the galvanic and hydrovoltaic effects drastically improves power generation performance. The device achieves a V_{OC} value of 0.65 V, an I_{SC} value of 4.33 μA, and a power density of 308 μW m^{-2}, representing 0.43-fold, 1.18-fold, and 10.84-fold increases, respectively, compared to the configuration without Fe electrodes. Recognizing that the film's evaporation performance is constrained by its water supply structure, we further regulate the width of the hydrophilic BFP strip used for water transport, as illustrated in Fig. 3f. As the BFP width increases from 0.5 cm to 2 cm, the surface evaporation rate rises from 0.44 to 1.16 kg m^{-2} h^{-1}, confirming that the water supply rate is a dominant factor governing evaporation behavior. However, further increasing the width to 3 cm yields only a marginal improvement, with the evaporation rate stabilizing at 1.18 kg m^{-2} h^{-1}. This saturation results from the limited photothermal conversion capacity of the CB/CNT@BFP film, which cannot support further evaporation beyond the rate enabled by its light absorption. In other words, the film's evaporation performance reaches a threshold once the water supply rate surpasses its photothermal driving capacity.

We systematically evaluate the hydrovoltaic performance of our design under various environmental conditions and working solutions, including pure water, dye-contaminated water, and seawater. First, we study the effect of solar intensity on electricity generation, as shown in Fig. 4a. As solar intensity increases, the output voltage rises steadily, indicating that enhanced photothermal heating promotes interfacial water evaporation. These results confirm that our modified design adapts well to different photothermal environments and benefits from synergistic photothermal effects. Next, we assess the device's applicability in different working media (Fig. 4b). The CB/CNT@BFP film generates electricity consistently in pure water, dye solutions, and seawater. Interestingly, the device exhibits higher output in dye-contaminated water than in pure water, which we attribute to increased ion concentrations that enhance charge separation and transport. Notably, the device also performs strongly in seawater, the most abundant water source on the Earth, achieving an output power density of 611 μW m^{-2} (Fig. 4c). It is worth noting that this electrical output is at least 8.5-fold higher than previously reported hydrovoltaic devices (Fig. 4d).[20,24–30] Our findings demonstrate that this functional film offers strong adaptability across a wide range of real-world aqueous environments. Additionally, we enhance the device's power output through series and parallel electrical connections (Fig. 4e). When four devices are connected in series, the open-circuit voltage reaches 4 V, and in a four-unit parallel configuration, the short-circuit current increases to ~15.6 μA (Fig. S10d, ESI†). We further evaluate the long-term stability of the device under solar irradiation (Fig. 4f). Over four consecutive 1-hour test cycles, the device maintains a stable output, with V_{OC} values consistently above ~1 V during each operation period. Even after 6 hours of continuous use, the film still generates a V_{OC} value of 0.8 V (Fig. S11, ESI†), confirming the excellent durability and operational stability of our hybrid platform.

In pursuit of optimal temperature oscillations for pyroelectric power generation, we introduce an arched structure into the upper layer of the multifunctional film to expand the evaporation area. To determine the optimal bending geometry, we evaluate the interfacial evaporation rate of films with different bending angles under 1 sun illumination (25 °C, 55% RH), as

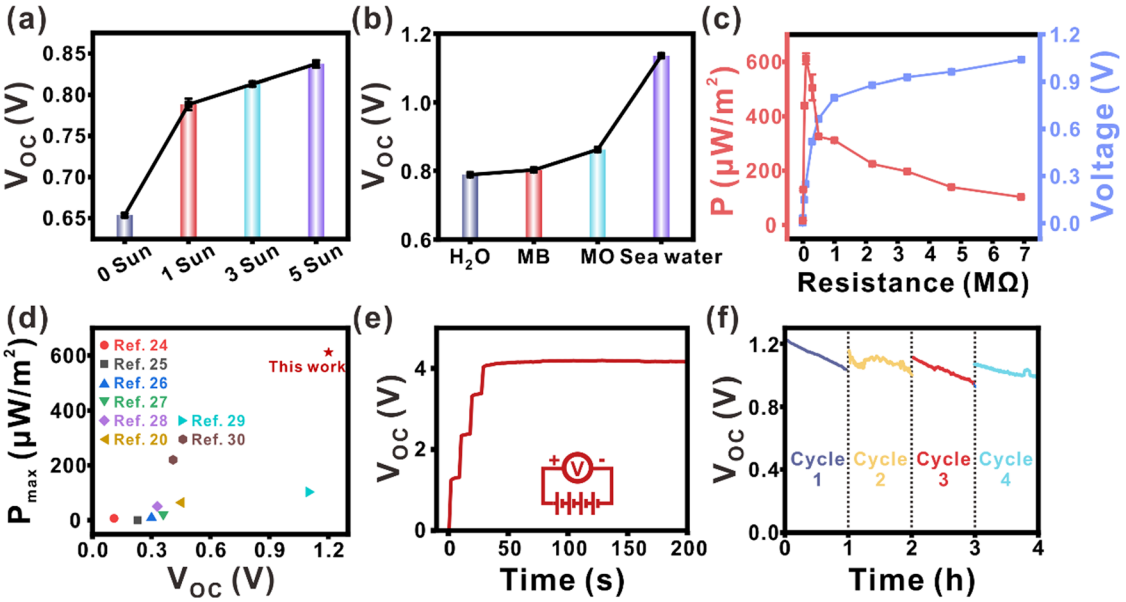

Fig. 4 Hydrovoltaic performance of the CB/CNT@BFP film under various environmental conditions. (a) Output voltage under different solar irradiation intensities (0–5 suns). (b) Hydrovoltaic voltage response in various working solutions (MB: 0.05 mg mL^{-1}; MO: 0.05 mg mL^{-1}). (c) Output power density (left panel) and voltage (right panel) of the hydrovoltaic generator in seawater under different external load resistances (1–7 MΩ). (d) Comparison of the maximum output power density of the hydrovoltaic device in this work with other reported designs. (e) V_{OC} of the device under four serial connection conditions. (f) Four repeated testing cycles of electrical performance, each lasting 1 hour.

shown in Fig. 5a. As the bending angle increases from 60° to 120°, the film surface becomes flatter, and the evaporation rate steadily rises. At 120°, the film reaches peak photothermal evaporation performance with an evaporation rate of ~1.53 kg m^{-2} h^{-1} and a calculated efficiency (η) of ~96%, which is ~7% higher than our previous CB-based design.[20] Notably, the evaporation rate declines beyond 120°. These results suggest that small bending angles limit sunlight exposure across the film, while excessive bending reduces the effective evaporation surface area. To further understand this behavior, we monitor surface temperature fluctuations caused by water phase transitions using a real-time temperature sensor (Fig. 5b). The fluctuation

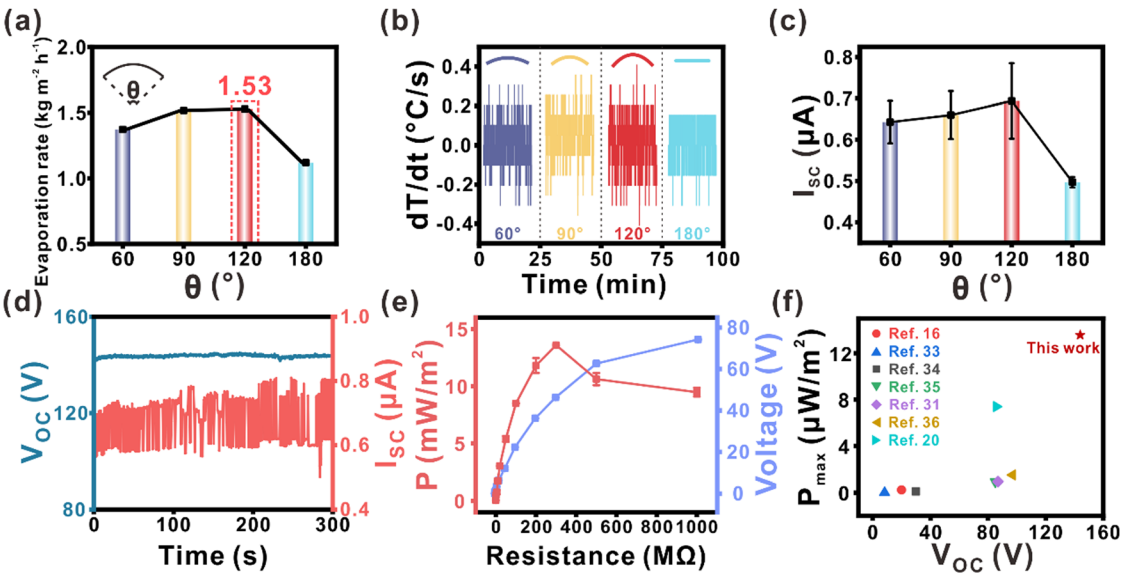

Fig. 5 Evaluation of pyroelectric performance in the hybrid platform with varying geometric configurations. (a) Photothermal evaporation rate of the CB/CNT@BFP layer with different bending angles and the (b) corresponding rate of surface temperature change. (c) Pyroelectric I_{SC} generated under different geometric curvatures. (d) Time-dependent V_{OC} (left) and I_{SC} (right) of the optimal device (120° bending) measured over 300 s under 1 sun illumination. (e) Pyroelectric power density (left panel) and voltage (right panel) under varying resistance loads (1–1000 MΩ). (f) Comparison of the maximum pyroelectric output power density of our design with previously reported systems.

magnitude increases with the bending angle and peaks at 120°, then sharply decreases at 180°, following the same trend as the evaporation rate. This correlation confirms that surface temperature variation is primarily driven by interfacial evaporation. We further validate this through pyroelectric current output measurements, which show a strong positive correlation with the rate of temperature change (Fig. 5c). These observations identify 120° as the optimal curvature angle for our multifunctional film to maximize both evaporation and temperature oscillation. These thermal oscillations activate the pyroelectric response of the polarized PVDF film beneath. The fluctuating temperature modulates the dipole alignment in the PVDF's β-phase crystalline domains, leading to a dynamic change in spontaneous polarization. This change generates transient currents and voltages as charges are redistributed, contributing additional electrical output.[31,32] We also investigate the stability of pyroelectric output in the optimized design after rectification over a 300-second cycle (Fig. 5d). The device maintains a steady V_{OC} of ~143 V and an I_{SC} of ~694 nA, confirming consistent pyroelectric power generation. Under this configuration (Fig. 5e), the device delivers a peak pyroelectric power density of 13.58 mW m^{-2}, which exceeds that of the planar film by over 80% and surpasses previously reported values (Fig. 5f).[16,20,31,33–36]

Notably, our hybrid design demonstrates superior power output performance to previously reported platforms in both hydrovoltaic (HV) and pyroelectric (PE) generation metrics, as benchmarked in Table S1 (ESI†). Moreover, when compared to thermoelectric (TE) generators based on Seebeck effect, the power output of HV and PE is significantly lower due to the differences in their power generation mechanisms. Nonetheless, our dual-mode design has higher output voltages (without the need for additional voltage boosting modules) and enables near-continuous electricity generation, ensuring sustained power output regardless of solar conditions (unlike TE which relies heavily on solar power). Therefore, our design is more conducive to practical deployment scenarios.

To demonstrate the practical potential of our platform, we first evaluate the power supply capability of the hybrid generator in real-world applications, including capacitor charging and powering small electronic devices. The device structure and operation process are shown in Fig. 6a. The arched hybrid generator simultaneously produces hydrovoltaic and pyroelectric electricity when exposed to seawater and solar illumination. The generated electricity is collected through front/rear and left/right electrodes and stored in capacitors. As pyroelectric output is alternating in nature, we rectify it into direct current before use. Moreover, we investigate the charging behavior of different capacitors using both hydrovoltaic and pyroelectric outputs (Fig. 6b and c). For hydrovoltaic performance, four generators connected in series rapidly charge capacitors ranging from 4.7 to 100 μF, reaching a stable voltage of 4 V within 5 minutes (Fig. 6b). Meanwhile, the pyroelectric output charges a 33 μF capacitor to over 20 V within 100 minutes (Fig. 6c). These results confirm that the harvested electricity is sufficient to power small devices, including three LEDs connected in series, a standard calculator (Fig. S13, ESI†), and an electronic watch (Fig. S14, ESI†). We further apply the hybrid generator in a self-driven electrocatalytic system by coupling it with commercial Pt electrodes to extract energy from seawater and

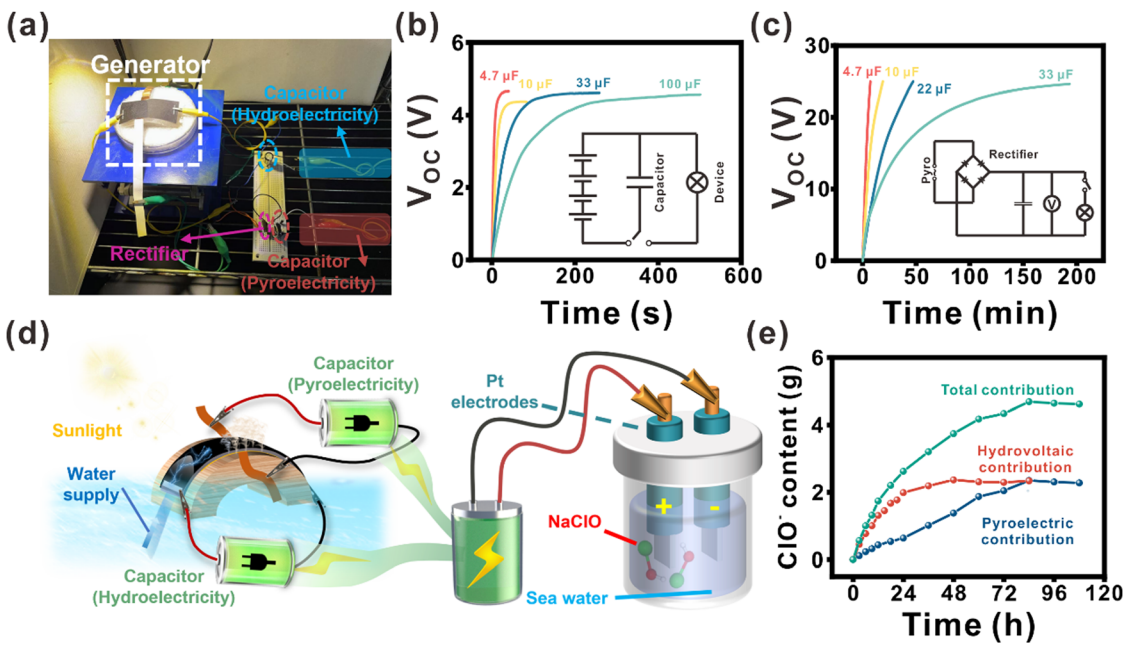

Fig. 6 Demonstration of the CB/CNT@BFP hybrid generator and its practical applications. (a) Optical images of the hybrid generator used for charging various capacitors. (b) V_{OC} of the capacitor charged by a hydrovoltaic power output. (c) V_{OC} of the capacitor charged by a pyroelectric power output. (d) Schematic illustration of the hybrid generator applied for electrocatalytic seawater decomposition. (e) Yield of self-powered disinfectant synthesis (sodium hypochlorite) driven by the hybrid generator.

synthesize disinfectants (Fig. 6d). We use a residual chlorine detector to quantify the yield of hypochlorite ions (ClO^-) produced through electrolysis. After 72 hours of seawater electrolysis, our self-powered hybrid generator achieves ClO^- concentrations of 2.31 and 2.35 g, respectively (Fig. 6e).

4. Conclusions

In this work, we have demonstrated a high-performance hybrid generator that efficiently harvests energy from water using a multiscale structural design. The optimized architecture achieves a photothermal evaporation rate of $\sim$1.53 kg m^{-2} h^{-1} with a conversion efficiency of $\sim$96%, $\sim$30% higher than that of a planar configuration, enabled by rational component-level regulation. The hydrovoltaic output reaches a V_{OC} of $\sim$1.13 V and an I_{SC} of $\sim$6.46 μA, delivering a power density of $\sim$611 μW m^{-2} which represents an 8.5-fold enhancement over previous designs under similar one sun illumination in seawater. Additionally, the multifunctional generator exhibits strong pyroelectric performance, achieving a V_{OC} of $\sim$143 V, an I_{SC} of $\sim$694 nA, and a peak power density of $\sim$13.58 mW m^{-2}, surpassing prior reports by over 80% due to enhanced temperature oscillations enabled by the arched design. The hybrid platform reliably powers small electronic devices, such as LED lamps and calculators, under ambient conditions. As a proof of concept, we further construct a self-driven electrocatalytic system for disinfectant synthesis by coupling the hybrid generator with commercial Pt electrodes. This integrated device successfully produces $\sim$4.67 g of sodium hypochlorite after 72 hours of seawater operation. This work offers a versatile and scalable strategy for constructing self-sustaining energy systems that harvest and convert water-derived energy into usable electrical output, paving the way for autonomous real-world applications in environmental remediation, disinfection, and off-grid chemical production.

Author contributions

Hui Cheng: methodology, data curation, visualization, investigation, formal analysis, and writing – original draft; Hiang Kwee Lee: conceptualization, formal analysis, writing – review & editing, and supervision; Haitao Li: conceptualization, funding acquisition, resources, writing – review & editing, supervision, and validation.

Conflicts of interest

The authors declare that they have no conflicts of interest.

Data availability

Data sharing is not applicable to this article as no new data were created or analyzed in this study.

Acknowledgements

Haitao Li acknowledges the financial support from the National Natural Science Foundation of China (52403278) and the Fundamental Research Funds for the Central Universities (RENCAI2025006) and Natural Science Foundation of Shandong Province (ZR2023QF019). H. K. L. acknowledges the funding support from the Singapore Ministry of Education (RS13/20 and RG4/21), the Agency for Science, Technology and Research, Singapore (A*STAR, A2084c0158), the Center of Hydrogen Innovation, the National University of Singapore (CHI-P2022-05), and the Nanyang Technological University start-up grants.

References

1 H. Wei, L. Zhou, F. Cao, Y. Chen, B. Li, J. Kou, C. Lu and Z. Xu, *Nano Energy*, 2024, **129**, 110064.
2 X. Xin, Y. Zhang, R. Wang, Y. Wang, P. Guo and X. Li, *Nat. Commun.*, 2023, **14**, 1759.
3 P. Duan, C. Wang, Y. Huang, C. Fu, X. Lu, Y. Zhang, Y. Yao, L. Chen, Q.-C. He, L. Qian and T. Yang, *Nat. Commun.*, 2025, **16**, 239.
4 S. Li, Y. Wang, Z. Liu, B. Chen, M. Liu, X. He and S. Yang, *Sci. Adv.*, 2025, **11**, eadt6136.
5 Y. Huang, T. Zheng and J. Wu, *Nano Energy*, 2024, **131**, 110184.
6 S. Lal, S. K. Batabyal, E. Wang and B. Hwang, *Chem. Eng. J.*, 2025, **505**, 159281.
7 R. A. Surmenev, R. V. Chernozem, I. O. Pariy and M. A. Surmeneva, *Nano Energy*, 2021, **79**, 105442.
8 T. Hu, K. Zhang, W. Deng and W. Guo, *ACS Nano*, 2024, **18**, 23912–23940.
9 L. Li, X. Sun, J. Miao, H. Wang, Y. Song and D. Tang, *Energy Environ. Sci.*, 2025, **18**, 1176–1190.
10 B. Shao, Y. Song, Z. Song, Y. Wang, Y. Wang, R. Liu and B. Sun, *Adv. Energy Mater.*, 2023, **13**, 2204091.
11 Y. Wang, C. Yang, X. Zhou, Y. Zuo, Z. Zhao and H. Chen, *Carbon*, 2024, **223**, 119008.
12 Y. Wang, X. Yuan, K. Ni, Y. Song, X. Li, X. Zeng, B. Shao and B. Sun, *Energy Environ. Sci.*, 2024, **17**, 4780–4793.
13 W. Yuan, H. Liu, Y. Fu, Y. Zhang, H. Huo, L. Zhang, M. Yang, Y. Li, C. Chen, Y. Song and Z. Ling, *Chem. Eng. J.*, 2024, **499**, 155952.
14 F. Gao, W. Li, X. Wang, X. Fang and M. Ma, *Nano Energy*, 2016, **22**, 19–26.
15 J. Han, S. Shin, S. Oh, H. J. Hwang, D. Choi, C. Lee and Y. Nam, *Nano Energy*, 2024, **126**, 109682.
16 M. Jiang, Q. Shen, J. Zhang, S. An, S. Ma, P. Tao, C. Song, B. Fu, J. Wang, T. Deng and W. Shang, *Adv. Funct. Mater.*, 2020, **30**, 191481.
17 L. Kong, Z. Qiu, Y. Wang, Y. Xie and Z. Xiao, *Carbohydr. Polym.*, 2025, **347**, 122727.
18 H. Liu, L. Liu, Z. Fan, J. Liu, H. Wang, X. Wen, G. Hu, K. Liu, R. Niu and J. Gong, *Chem. Eng. J.*, 2024, **485**, 149690.
19 R. Xiao, X. Zhou, T. Yang, Z. Liu, S. Han, J. Wang, H. Wang and D. Ye, *Nano Energy*, 2025, **136**, 110759.

20 H. Li, H. Cheng, B. Wu, W. Wang, Y. Zhang and J. Han, *Chem. Eng. J.*, 2024, **495**, 153497.
21 W. Duan, Z. Sun, X. Jiang, S. Tang and X. Wang, *Nano Energy*, 2025, **134**, 110516.
22 Y. Wang, C. Wang, X. Song, S. K. Megarajan and H. Jiang, *J. Mater. Chem. A*, 2018, **6**, 963–971.
23 J. Tan, X. Wang, W. Chu, S. Fang, C. Zheng, M. Xue, X. Wang, T. Hu and W. Guo, *Adv. Mater.*, 2024, **36**, 2211165.
24 S. Chaurasia, R. Kumar, T. Tabrizizadeh, G. Liu and K. Stamplecoskie, *ACS Omega*, 2022, **7**, 2618–2623.
25 G. Xue, Y. Xu, T. Ding, J. Li, J. Yin, W. Fei, Y. Cao, J. Yu, L. Yuan, L. Gong, J. Chen, S. Deng, J. Zhou and W. Guo, *Nat. Nanotechnol.*, 2017, **12**, 317–321.
26 M. Li, L. Zong, W. Yang, X. Li, J. You, X. Wu, Z. Li and C. Li, *Adv. Funct. Mater.*, 2019, **29**, 1901798.
27 Z. Liu, J. Xie, J. Xu, Q. Wang and G. Liu, *Electrochim. Acta*, 2024, **477**, 143742.
28 J. Y. Park, Y. Kwak, J.-E. Lee, Y.-D. Kim, S.-H. Lee, D.-W. Jeong, B.-S. Kim and Y.-H. Choa, *Chem. Eng. J.*, 2024, **485**, 149914.
29 T. A. Wani, D. Kim, J. Choi, M. Song and S. Jeon, *ACS Appl. Eng. Mater.*, 2024, **2**, 2433–2441.
30 J. Zhang, P. Cui, J. Wang, H. Meng, Y. Ge, C. Feng, H. Liu, Y. Meng, Z. Zhou, N. Xuan, B. Zhang, G. Cheng and Z. Du, *Adv. Sci.*, 2023, **10**, 2304482.
31 H. Li, H. Wang, X. Li, J. Huang, X. Li, S. K. Boong, H. K. Lee, J. Han and R. Guo, *Nano Energy*, 2022, **100**, 107527.
32 Z. Lin, X. Guo, Z. Wang, B. Wang, S. He, L. A. O'Dell, J. Huang, H. Li, H. Yu and L. Chen, *Nano Energy*, 2020, **73**, 104786.
33 T. Ding, L. Zhu, X. Q. Wang, K. H. Chan, X. Lu, Y. Cheng and G. W. Ho, *Adv. Energy Mater.*, 2018, **8**, 1802397.
34 X.-Q. Wang, C. F. Tan, K. H. Chan, K. Xu, M. Hong, S.-W. Kim and G. W. Ho, *ACS Nano*, 2017, **11** 10568–10574.
35 L. Zhu, M. Gao, C. K. N. Peh, X. Wang and G. W. Ho, *Adv. Energy Mater.*, 2018, **8**, 1702149.
36 H. Wang, L. S. Ng, H. Li, H. K. Lee and J. Han, *Nano Energy*, 2023, **108**, 108184.

